



**HAL**  
open science

## Designing plasmonic eigenstates for optical signal transmission in planar channel devices

Upkar Kumar, Sviatlana Viarbitskaya, Christian Girard, Aurelien Cuche, Sreenath Bolisetty, Raffaele Mezzenga, Gérard Colas Des Francs, Alexandre Bouhelier, Erik Dujardin

► **To cite this version:**

Upkar Kumar, Sviatlana Viarbitskaya, Christian Girard, Aurelien Cuche, Sreenath Bolisetty, et al.. Designing plasmonic eigenstates for optical signal transmission in planar channel devices. 2017. hal-01628475v1

**HAL Id: hal-01628475**

**<https://hal.science/hal-01628475v1>**

Preprint submitted on 3 Nov 2017 (v1), last revised 5 Sep 2018 (v3)

**HAL** is a multi-disciplinary open access archive for the deposit and dissemination of scientific research documents, whether they are published or not. The documents may come from teaching and research institutions in France or abroad, or from public or private research centers.

L'archive ouverte pluridisciplinaire **HAL**, est destinée au dépôt et à la diffusion de documents scientifiques de niveau recherche, publiés ou non, émanant des établissements d'enseignement et de recherche français ou étrangers, des laboratoires publics ou privés.

# Designing plasmonic eigenstates for optical signal transmission in planar channel devices

Upkar Kumar,<sup>1</sup> Sviatlana Viarbitskaya,<sup>2</sup> Christian Girard,<sup>1</sup> Aurélien Cuche,<sup>1</sup> Sreenath Bolisetty,<sup>3</sup> Raffaele Mezzenga,<sup>3</sup> Gérard Colas des Francs,<sup>2</sup> Alexandre Bouhelier,<sup>2</sup> \* Erik Dujardin<sup>1</sup> \*

<sup>1</sup> CEMES CNRS UPR 8011, 29 rue J. Marvig, 31055 Toulouse, France.

<sup>2</sup> Laboratoire Interdisciplinaire Carnot de Bourgogne, CNRS UMR 6303, Université de Bourgogne Franche-Comté, 9 Av. A. Savary, 21000 Dijon, France.

<sup>3</sup> ETH Zurich, Department of Health Sciences and Technology, Schmelzberg-strasse 9, CH-8092 Zurich, Switzerland

\* Corresponding authors: dujardin@cemes.fr, alexandre.bouhelier@u-bourgogne.fr

## Abstract

On-chip optoelectronic and all-optical information processing paradigms require compact implementation of signal transfer for which nanoscale surface plasmons circuitry offers relevant solutions. This work demonstrates the directional signal transmittance mediated by 2D plasmonic eigenmodes supported by crystalline cavities. Channel devices comprising two mesoscopic triangular input and output ports and sustaining delocalized, higher-order plasmon resonances in the visible to infra-red range are shown to enable the controllable transmittance between two confined entry and exit ports coupled over a distance exceeding  $2\ \mu\text{m}$ . The transmittance is attenuated by  $> 20\text{dB}$  upon rotating the incident linear polarization, thus offering a convenient switching mechanism. The optimal transmittance for a given operating wavelength depends on the geometrical design of the device that sets the spatial and spectral characteristic of the supporting delocalized mode. Our approach is highly versatile and opens the way to more complex information processing using pure plasmonic or hybrid nanophotonic architectures.

Signal transfer at faster rates, longer distances, along narrower pathways, with reduced losses and a higher bandwidth are some crucial impediments to the improvement of any information processing technologies. Optical transfer in free space, dielectric waveguides or fibers offers the best prospects for several of these criteria except for sub-wavelength spatial confinement. Yet, this particular point is of paramount importance to interface optical signal with electronic information processing and has been partially addressed by the photon-plasmon conversion using noble metal circuitry.<sup>1-6</sup> Surface plasmon (SP) propagated in films,<sup>7,8</sup> waveguided in grooves<sup>9-11</sup> or stripes<sup>12-14</sup> has proven efficient in transmitting or even processing information to and from optical and optoelectronic planar devices.<sup>15-17</sup> The optoelectronic conversion has become more challenging as the size of electronic devices is reaching the nanoscale though recent advanced functionalities based upon particle chains<sup>18,19</sup> and atomic-size gaps<sup>20-25</sup> could allow the next level of downsizing. Notably, even at the nanoscale, the dominant approach to signal transmission consists in propagating along a selected wave vector or inside a one-dimensional (1D) waveguide, but lossy in- and out-coupling usually limit the overall transfer efficiency.<sup>26,27</sup> A further step is to design the spatial distribution of the in-plane plasmon modes to implement the in-, out-coupling as well as the directional transmission functions. The use of spatial and spectral properties of higher order plasmon modes in 2D crystalline Au cavities have recently been proposed as a generic scattering loss free approach to integrated optical logic gates and, further, information processing.<sup>28</sup> The implementation of plasmonic devices from the properties of 2D cavity modes pertain to the ability to tailor their size and shape.<sup>29-31</sup> While simple and usually symmetrical shapes can be obtained directly by chemical synthesis, the full potential of arbitrarily shaped cavities can, so far, only be attained by the physical or chemical etching of crystalline Au platelets which has already led, for example, to antennas with improved performances.<sup>32,33</sup> Using this approach, we have recently demonstrated that a small defect, such as a hole, could significantly alter the modal behavior of 2D cavities pointing out the potential for more complex modal design.<sup>34</sup>

Here, we report the directional signal transmittance mediated by the rich and complex spatial and spectral variation of the plasmonic eigenmodes supported by 2D crystalline structures. The potential of multiple input-output devices with a controllable transmission between one entry and one exit ports is demonstrated in a diabolo-like structures composed of a rectangular channel flanked by two mesoscale triangular pads that sustain higher order modes in the visible spectral range,<sup>28,35</sup> as schematized in Figure 1. The size of the structure is intermediate between the supra- and sub-wavelength size ranges so as to combine long range delocalization and sharp field enhancement at the input and output ports that are therefore precisely defined. In Figure 1c, an in-plane near-field intensity map is calculated over the entire diabolo for an optical excitation consisting of a Gaussian laser beam impinging on the structure at normal incidence. The beam is kept fixed at one corner of the triangular input cavity. A clear remote response is observed at the output cavity as far as the diagonally opposed corner. The full map suggests that the remote response is mediated by the excitation of a mode bridging the input and output locations via the channel. Interestingly, the output signal is almost annihilated when the incident polarization is rotated by 90° (Fig. 1d). The same near-field transmittance simulations provide the spectral distribution of the delocalized plasmon modes (Fig. 1b). The

simulated transmittance spectra are monitored in (O) when the diablo is excited with horizontal or vertical polarizations in (I). Upon horizontal polarization excitation (black curve), the symmetrical diablo exhibits a 100-nm wide transmittance peak culminating at 810 nm. When the polarization is flipped (red curve), the spectrum is completely attenuated near this spectral region. These simulations strongly suggest that the transmittance is obtained by populating polarization-dependent 2D delocalized modes. Indeed by simply moving the excitation to the lower corner of the input cavity, the signal is redirected to the upper corner of the diablo output cavity through a symmetrical set of delocalized eigenstates. We experimentally explore this concept and demonstrate the effective spectral and spatial engineering of higher order plasmon modes in channel devices comprising input and output cavities. These information transfer structures may comply with the upcoming demand of compact processing devices, such as logic gates,<sup>27,36</sup> coupled to quantum emitters in integrated architectures aimed at transferring<sup>6,37,38</sup> and manipulating<sup>39,40</sup> quantum information.

Focused ion beam (FIB) milling etching of crystalline gold microplatelets is used to fully design a structure supporting cavity modes that can be spatially and spectrally optimized to perform the desired transmission function from a chosen input port to a specific output location (Fig. 2a). This nanofabrication method provides plasmonic nanocircuits and devices with superior structural and optical quality.<sup>32</sup> The microplatelets are synthesized by a simple green reducing process reported in reference<sup>41</sup>. The colloidal suspension is drop-casted onto cross-marked glass coverslip and thoroughly washed. The microplatelets are natively stabilized by strongly adsorbed  $\beta$ -lactoglobulin amyloid fibrils, which are removed by three successive O<sub>2</sub>-plasma treatments. We conducted scanning electron microscopy (SEM) and atomic force microscopy (AFM) to assess the scarce density of colloidal objects on the surface in order to address single objects. The in-plane dimensions ( $\sim$  2-3  $\mu$ m) and thickness (20-40 nm) of the targeted native hexagonal microplatelets are recorded individually (Fig. 2b). Gallium ion FIB milling is performed, first, to etch out the diablo shape (Fig. 2c) and then to remove the peripheral fragments of the mother microplatelet. The milling protocol is optimized using a pattern generator and nanolithography software to reduce edge amorphisation, metal re-deposition and gallium contamination. The typical side length of the equilateral triangular pads ranges from 600 to 1000 nm, which is comparable to chemically synthesized prismatic cavities, and the connecting channel is 500 nm long and 200 nm wide (See Experimental Section).<sup>42</sup>

Non-linear photoluminescence (nPL) microscopy is a convenient technique to easily map out the intensity of the local field inside plasmonic devices without resorting to slow and invasive near-field scanning probes.<sup>28,43</sup> nPL imaging acts as a local probe that benefits from a higher spatial resolution and sensitivity conferred by the non-linear mechanism. In this work, the nPL of gold is excited with a 180-fs pulsed Ti:Sapphire laser focused in a diffraction-limited spot by a high numerical aperture objective (N.A. 1.49). The excitation spot diameter is about 300 nm and the mean power density at the sample is 20 mW. $\mu$ m<sup>-2</sup>. The power dependency of the non-linear emission signal collected in the 375–700 nm spectral range is quadratic and assimilated as such in corresponding simulations. Two different nonlinear optical mapping modes are implemented to obtain the modal landscape and the transmittance of the device (See Experimental Section and Fig. S2). The first mode provides confocal maps reconstructed by raster scanning

the device through the focal spot. The intensity of the detected nPL is proportional to the squared in-plane surface plasmon local density of states (SP-LDOS) and the map reveals the spatial distribution of the modal structure of the 2D confined plasmons (Figs. S3 and S4).<sup>28</sup>

In the second imaging mode, the nPL response of the entire device is recorded for a fixed excitation position to visualize the plasmon-mediated signal transfer and distant nPL generation within the device.<sup>44</sup> Such wide-field images, displayed in Figures 2d and 2e, are obtained when the diabolos shown in Fig. 2a is excited in position (I) for two orthogonal linear polarizations of the excitation beam. In Figure 2d, nPL is not only observed as a local response coinciding with the excitation spot but also from several remote regions of the input triangle, the channel and even from the distant corner of the right triangle, where a localized bright spot can be observed in position (O). The nPL distribution recorded in Figure 2d matches faithfully the transmittance map calculated in Figure 1c, thus providing a compelling correlation between the transmission of the near-field from a fixed excitation and the remote production of nPL signal. The nPL images suggest that the pulsed excitation in (I) is indeed carried through the channel, as was recently observed in straight micrometer-long rods.<sup>44</sup> Yet, in contrast to long rods, which sustain a continuum of accessible resonances, the non-linear emission from the diabolos is not uniformly scattered from the remote (right) edge but it emerges from a very localized and specific location close to the corner, which coincides with an antinode of the SP-LDOS distribution (see Fig. 3a). This remote output spot could be used to further excite a collecting waveguide, forming an all-optical switch in an integrated nanophotonic platform.<sup>36,45</sup> A comparison of the image plane and confocal nPL maps confirms that the transmittance takes place between two locations of high SP-LDOS intensity, i.e. showing intense confocal nPL signal (see Supplementary information Figs. S3 and S4). Indeed, the discrete modal structure of the diabolos is revealed in the computed maps of the projected in-plane SP-LDOS (Fig. 3 a-d) and the simulated nPL maps for an incident linearly polarized beam with a waist of 300 nm (Fig. 3 e-h). In particular, the four extremal hotspots in the corners of the triangular pads (Fig. 3e) are reminiscent of the ones observed in crystalline triangular prisms.<sup>28</sup> The input (I) and output (O) should be chosen in registry with these hotspots but the confocal nPL maps do not provide the transmittance connectivity between them. The simulated SP-LDOS map in Fig. 3a suggests a connecting modal path enabling a transfer of plasmon information through the channel, when the SP-LDOS is projected along the horizontal linear polarization. The transmission configurations with horizontally polarized excitation (Figs. 1c and 2d) reveal that the four corners of the diabolos are connected in pairs by two energetically degenerated and diagonally delocalized modes that mediate the effective transmittance between (I) and (O) only or, similarly, between (I') and (O') only. In the confocal nPL maps (Fig. 3f-h), the relative intensity of the spots is adjusted by rotating the polarization direction away from horizontal. Hence, an excitation with a vertical polarization does not result in a bright nPL emission from the distal tip of the triangular cavity as previously observed in the case of isolated prisms of similar size,<sup>28,30</sup> but in a strongly reduced emission from the proximal corner and channel (Fig. 3f) associated with a minimal SP-LDOS distribution within the channel (Fig. 3b). In Figure 2e, this polarization configuration for the beam parked in input (I) markedly alters the intensity distribution transmitted in output (O) wherefrom no nPL emission is recorded. This is again in very good agreement with the simulated near-field transmittance map shown in Figure 1d. The effective

signal transmittance for a horizontally polarized excitation and its variation upon rotating the polarization by  $90^\circ$  are further compared in Figure 2f by the intensity profiles plotted along the same I-C<sub>i</sub>-O dotted path in Fig. 2a. While the confocal emission intensity in (I) is only reduced by 55%, the transmittance modulation ON/OFF ratio in (O) reaches 130 or 21 dB.

Figures 2 and 3 indicate that the transmittance is enabled by a spatial and spectral excitation of plasmonic eigen-modes of the diablo. To further confirm the mode-mediated signal transfer, we considered exciting the structure in other locations while monitoring the non-linear emission at the output port (O) of the device. For example, in Figure 4, the excitation beam is parked at the left entrance of the channel (channel input point C<sub>i</sub>, in Fig. 2a) which results in a striking change of behavior compared to the excitation in (I). A horizontally polarized excitation does not produce any delocalized nPL emission from the right pad (Fig. 4a) while a vertical polarization generates both an intense emission at the excitation point and a remote nPL spot in (O) as seen in the inset of Figure 4b. The corresponding simulated near-field SP transmittance maps are presented in Figures 4c and 4d for horizontally and vertically polarized excitation in C<sub>i</sub>, with insets showing a 10x magnified intensity maps of the output regions. Both the relative intensity distributions and the spatial emission patterns observed in the nPL images are faithfully accounted for in the transmittance maps. The change of transmittance is clearly observed in the experimental intensity I-C<sub>i</sub>-O profiles plotted in Figure 4e. A  $90^\circ$  polarization flip is accompanied by a 9.0-fold increase of the confocal emission but only induces an ON/OFF ratio of 3.2 in spite of the (C<sub>i</sub>)-(O) geometric distance ( $\sim 1.1 \mu\text{m}$ ) being about half the (I)-(O) distance ( $\sim 1.9 \mu\text{m}$ ). Significant dissipation effects that would limit the plasmon propagation can thus be excluded. In light of the computed maps of Fig. 3, we attribute this reduced transmittance efficiency to low density of states at point (C<sub>i</sub>), which makes the energy in-coupling less effective. Interestingly, the polarization dependence of the transmittance when directly exciting the entrance of the channel at (C<sub>i</sub>) is orthogonal to the case of a beam impinging in (I). This counter-intuitive behavior indicates that in spite of its shape, the channel cannot be considered as a rod nor the diablo as the simple juxtaposition of two triangular and a rod-shaped sub-structures. The diablo sustains specific resonances, the spatial distribution of which specifically enables the transport of plasmon information from a high SP-LDOS area to another via the mediation of the finite SPLDOS present in the channel. This is precisely modelled in our plasmon transmittance simulation tool, in which the effective transmittance dependence on the existence or not of a phase matching throughout the device (See Supplementary Information, section 6).<sup>19</sup> In Figure 4f, the transmittance of the device calculated for inputs (I) or (C<sub>i</sub>) and output (O) is compared to the corresponding experimental nPL intensity measured in image plane maps for the two polarization configurations. The transmittance calculations faithfully follow the relative intensity of the output nPL intensity, which is maximized for the horizontal polarization when exciting in (I) and by the vertical polarization when exciting in (C<sub>i</sub>). Moreover, the near-field SP and nPL output transmittance in (O) in Figure 4f match the relative variation of the confocal nPL intensities in Figures 3 and S4 suggesting that the major contribution to the transmittance variation comes from the in-coupling efficiency. Indeed, a lower nPL intensity in (C<sub>i</sub>) is measured for the horizontal polarization (Figs. 3e and S4a) than for the vertical polarization

(Figs. 3f and S4b), while the opposite is observed in (I). The efficiency to generate a non-linear output varies in other locations and is provided by the confocal nPL maps in Figures 3e-f. Some minor relative differences between the simulated and experimental transmittances are ascribed to the fact that our transmission model computes the linear near-field rather than the non-linear emission and does not account for the full complexity of the out-coupling to the farfield and nPL collection, which may vary from one excited modes and for a particular polarization to another.

The operation of the transfer devices at a given energy relies on the spatial and spectral tailoring of a supporting delocalized mode that simultaneously enables an effective transmission and localized in- and out-coupling. This spatial and spectral matching of the cavities can be altered by varying the global geometry of the device. For instance, the symmetry breaking created in bowtie-like antennas comprising two mesoscale triangular prisms with different sizes was shown to have a marked effect on the local field distribution and spectral response.<sup>35</sup> We have fabricated non-symmetrical diabolos by changing the relative sizes of the triangular pads while keeping the same channel geometry. In Figure 5, we examine the case of a structure made of a 640-nm left side triangular pad connected to a 730-nm right side triangular pad (Fig. 5a). The total in-plane SPLDOS plotted in Figure 5b highlights the non-symmetrical modal structure with a predominant  $m=3$  mode on the left side and a predominant  $m=5$  mode on the right side. When the diablo is excited at input (I) with a linearly polarized beam along the horizontal or vertical direction, no output is observed in (O) as shown in Figures 5c and 5d, even when the output data is magnified ten times. The series of experimental nPL profiles in Figure 5g demonstrates that the transmittance along the I-Ci-O path remains inhibited for all polarization directions. The incident excitation propagates as far as the mid-channel area but is completely suppressed in the right side of the device. As the incident polarization direction is rotated, one can notice that the intensity of the nPL is uniformly affected over the entire structure, in striking contrast to the periodic intensity redistribution observed with the symmetrical diablo for a similar sequence (See details in section 4 and Figure S5 of the Supplementary Information). The reshaping of the diablo keeps the system off-resonance and does not allow for a signal transmission through the channel. We confirm the transmittance suppression by calculating the near-field SP transmittance maps for horizontally (Fig. 5e) and vertically (Fig. 5f) polarized excitation in (I). Once again, a very good match with the corresponding experimental maps is obtained. In the excitation regions, the confined hotspot and the extension along the edges observed in Figure 5c are matched by the two intense lobes in Figure 5e, while the weak and diffuse signal around (I) in Figure 5d is also obtained in the simulated Figure 5f. Furthermore, in the output regions, both polarization configurations yield a weak signal, which is marginally more intense in Figure 5e (horizontal polarization) than in Figure 5f (vertical polarization), in agreement with the weak transmittance measured in Figures 5g and S5. The spatially modulated, long-range transmittance monitored in the nPL images merely reveal in space the spectral match or mismatch of the device with the excitation conditions. In Figure 5h, the smaller non-symmetrical diablo exhibits a sharper and blue-shifted transmittance peak at 775 nm (black curve) compared to the 820-nm resonance of the larger symmetrical device upon horizontally polarized excitation (Fig. 1b). Additionally, a low energy peak beyond 850 nm is observed in the non-symmetrical diablo for the orthogonal excitation (red curve). Both excitation

configurations though show a vanishing transmittance intensity at 810 nm, which confirms the off-resonance response of the non-symmetrical geometry at this wavelength. Similarly, the off-resonance excitation of the symmetrical diablo at 750 nm results in no detectable nPL and in marginal transmittance in simulated maps in the output port, as shown in section 6 of the Supplementary Information. The spectral differences between the two diabolos are both related to their shape differences and relative sizes, the non-symmetrical one comprising smaller triangular pads features resonances that are blue-shifted compared to the ones of the symmetrical device. Yet the smaller size itself does not warrant a higher transmittance which can be suppressed when operated out of resonance.

As a conclusion, our results illustrates how the modal engineering in two dimensions can be harnessed to design and optimize the optical signal transmission in compact and single crystalline devices that could be docked to other information processing modules. Here, we have shown that the structural design of 2D mesoscale resonators from crystalline gold platelets allows to spatially and spectrally engineer SP modes exhibiting both delocalized extension and strong spatial modulation. Diabolo structures composed of a transmission channel flanked by two triangular resonators are investigated in detail. The excitation of the diabolo structures at specific input sites with suitable wavelength and polarization results in a remote but confined response, therefore implementing an efficient multi input/output signal transmission through a two-dimensional device. The transmission mechanism is related to the existence of a complex plasmonic modal landscape. The transmission function is demonstrated experimentally using a fixed excitation and a detection of the spatial extension of the response through the channel. Our experimental results are confirmed numerically using a dedicated near-field SP transmittance code with a realistic polarized Gaussian excitation. The performances of the transmission modulation upon polarization flipping at 810 nm show a large ON/OFF ratio of 20dB for the spectrally-matched symmetrical diabolo and an overall transmission efficiency of 3.5% at 2  $\mu\text{m}$  distance. Our modal design approach to engineer and modulate SP transmission in compact wavelength-size devices contribute to the recent strategies to embed active information processing functions into pure or hybrid plasmonic structures such as the insertion of phase changing material into gold transmission lines<sup>46</sup> or the ultrafast electrical switching of SP in indium tin oxide waveguides.<sup>47-49</sup> The diabolo structures examined in this work are merely one first example of the potential of modal engineering in pure plasmonic systems toward information processing and transfer in complex devices, which could be used to create new computing architectures for classical and quantum optical technology.<sup>37,38,50</sup>



## Experimental Section

**Sample preparation.** The crystalline gold microplatelets are synthesized using  $\beta$ -lactoglobulin protein fibrils according to the methods reported in references <sup>41,51</sup>. The microplatelets studied here are prepared by initial mixing of 0.01M HAuCl<sub>4</sub> salt with 0.6 wt% of  $\beta$ -lactoglobulin fibrils and then heated at 55° C for 24 hours. The microplatelets are 20-40 nm in thickness and the typical in-plane dimensions are in the range of 1-15  $\mu$ m. The colloidal suspension is drop-casted onto glass coverslips (22  $\times$  22  $\times$  0.15 mm) coated with a nominal 10-nm indium-tin oxide (ITO) layer. Cross-mark arrays are designed by photolithography and Au metallization. Organic residues are thoroughly washed with 10% aqueous ethanol solution and deionized water and the gold surface is decontaminated by three successive 5-min O<sub>2</sub> plasma treatments. The diabolo structures are fabricated by focused ion milling of hexagonal microplatelets with diameter of 3-5  $\mu$ m using a gallium ion beam on a Zeiss 1540 XB dual beam microscope interfaced with a Raith Elphy Multibeam pattern generator. To ensure minimal substrate milling while thoroughly etching the gold, typical ion current of 1.0 pA and dose of 8000  $\mu$ C.cm<sup>-2</sup> are used. The milling protocol consists in etching out the diabolo pattern first with minimal beam rastering along the diabolo edges. The peripheral portions of the starting hexagonal colloid are milled in a second step.

**Confocal and Image plane non-linear optical microscopy.** Confocal and Wide-field non-linear optical microscopy is performed on an inverted microscope. A 180 fs pulsed Ti:Sapphire laser tuned at  $\lambda = 810$  nm is focused in a diffraction-limited spot by a high numerical aperture objective (oil immersion, 100x, NA = 1.49). The full width half maximum (FWHM) spot diameter of the excitation beam is about 300 nm. The laser average power density at the sample is 20 mW. $\mu$ m<sup>-2</sup>. The linear polarization of the excitation beam is rotated by a half-wavelength plate inserted at the laser output. Non-linear photoluminescence (nPL) is collected through the same objective, as the sample is raster scanned with a XY piezo stage (step size 25-50 nm), and filtered in the 375–700 nm spectral range from the backscattered fundamental beam by a dichroic beam splitter and a collection filter. Confocal maps are recorded on an avalanche photodiode. Since the non-linear photoluminescence is quadratic with the excitation power, the experimental maps are normalized with the square of the excitation power measured at the back aperture of the objective. Direct plane wide-field images are collected in the absence of a spatial filter, allowing detection of signal emitted from the entire structure for a fixed excitation position. Compared to the confocal set-up, the pinhole in the conjugate image plane is removed and replaced by a CCD camera to record the magnified image of the diabolo structure.

**Simulations.** Numerical simulations of the local electromagnetic field, SP-LDOS and nPL signal were performed using home-made codes based on the 3D Green Dyadic Method as described in earlier reports.<sup>43</sup> The generalized propagator  $\mathbf{K}(\mathbf{r}, \mathbf{r}', \omega)$  is computed first that gives the total electromagnetic response of the complex metallic nanostructure under any arbitrary illumination field  $\mathbf{E}_0(\mathbf{R}_0, \mathbf{r}, \omega)$ . The diabolo nanostructure

is discretized into hexagonal lattice of cells. The local electromagnetic field inside the metallic nanostructure is then given by

$$\mathbf{E}(\mathbf{R}_0, \mathbf{r}, \omega) = \int_V \mathbf{K}(\mathbf{r}, \mathbf{r}', \omega) \cdot \mathbf{E}_0(\mathbf{R}_0, \mathbf{r}', \omega) d\mathbf{r}'$$

where  $\mathbf{R}_0$  represents the center of the light beam. Simulations of confocal nPL intensity generated by a Gaussian beam excitation are obtained by integrating the square of local electric near-field intensity on the whole structure. The computed nPL maps are constructed by raster scanning the position of the sample through the focused Gaussian beam.<sup>30,43</sup> The same formalism is used to calculate SPLDOS spectra and maps inside a metallic nanostructure.

The SP-LDOS transmittance calculations are performed with an excitation located at a fixed input co-ordinate (position vector  $\mathbf{r}_1$ ). The transmitted near-field intensity generated by the excited plasmonic field at a distal output co-ordinate (position vector  $\mathbf{r}_2$ ) is calculated. The energy transferred from input to output is obtained by solving the Dyson sequence equation which gives the Dyadic tensor  $\mathbf{S}(\mathbf{r}_2, \mathbf{r}_1, \omega)$ .

**Acknowledgements.** This work was funded by the French Agence Nationale de la Recherche (Grant ANR-13-BS10-0007-ANR-PLACORE), the region of Burgundy under the PARI II Photcom and the European Research Council under the FP7/ 2007-2013 Grant Agreement No. 306772. The authors acknowledge the support of the massively parallel computing center CALMIP (Toulouse, Fr).

**Competing financial interests.** The authors declare no financial competing interests.

**Author contributions:** ED, CG, AB designed the experiments. RM and SB synthesized the Au microplatelets. UK and ED conducted the sample preparation and nanofabrication steps. AB, SV implemented the experimental optical set-up. UK, SV, AC performed the optical experiments. CG, AC, UK, GCdF developed the simulations tools and performed all calculations. ED and UK processed the data. All authors contributed to the data analysis and manuscript writing.

**Supplementary Information.** Supplementary information is available in the online version. It comprises supplementary figures S1 to S9, supplementary sections S1 to S6 and supplementary references.

## Figure captions

**Figure 1.** Modal transmittance in mesoscopic crystalline gold, diabolo-shaped devices. **(a)** Scheme for the numerical computation of the transmittance through the eigenstates of a channel device connecting triangular cavities. A focused pulsed laser beam is parked on the top left corner of the device (I). The transmitted near-field is calculated in all locations along the entire structure. Particular attention is paid to the farthest point (O) indicated by the black dot. The underlying map is a 3D rendering of panel (c). **(b)** Transmittance spectra calculated in (O) for a diabolo comprising 925-nm sided input and output triangular pads and a 500 × 200 nm channel excited with a linearly polarized Gaussian beam at 0° (black circles) and 90° (red circles). **(c, d)** Corresponding simulated near-field transmittance maps. The white circles indicate the position of the realistic 300-nm diameter, Gaussian excitation spot ( $\lambda_{exc} = 810$  nm, dash-dotted line in (b)), which is linearly polarized at (b) 0° and (c) 90° (See Suppl. Info for details). The color scale is multiplied by 10 to emphasize the transmission through the channel toward the exit port (right side of the device),

**Figure 2.** Experimental demonstration of the modal transmittance in diabolo-shaped devices **(a)** Scanning electron microscopy (SEM) image of a symmetrical diabolo-shaped structure. The sample is composed of two identical triangles (side length 925 nm) connected by a 500-nm long, 200-nm wide channel. (I), (C<sub>i</sub>) and (O) indicated the specific input, channel input and output locations considered in this work. **(b)** SEM image of the pristine crystalline Au microplatelet deposited on ITO-coated glass coverslip prior to ion milling the sample shown in (a). **(c)** SEM image of the same microplatelet after nanopatterning the diabolo structure and prior to ion etching the unwanted peripheral parts of the starting platelet. **(d, e)** Non-linear photoluminescence (nPL) wide-field CCD image of the diabolo structure shown in (a) when the 810-nm excitation is placed in (I) for an incident beam polarized at (d) 0° and (e) 90°. The insets on the right display the signal from the output right triangular area with a 10x magnified color scale. **(f)** nPL profiles extracted from (d) and (e) along the path indicated by the dash-dotted line in (a). Inset: Magnified plot of the output (O) region corresponding to the dotted box in the main graph. Scale bars are (a, d, e) 200 nm and (b, c) 1  $\mu$ m.

**Figure 3.** Plasmon modal properties of the mesoscale diabolo structure. **(a-d)** Partial in-plane SP-LDOS maps calculated for the symmetrical diabolo structure shown in Fig. 2a at  $\lambda = 810$  nm and projected along linear polarization at (a) 0°, (b) 90°, (c) 120° and (d) 150°. **(e-h)** Simulated confocal nPL maps for a  $\lambda = 810$  nm, linearly polarized excitation at (e) 0°, (f) 90°, (g) 120° and (h) 150°. The common scale and color bars are shown in (a) and (e) is 200 nm.

**Figure 4.** Direct channel excitation. **(a, b)** Non-linear photoluminescence wide-field CCD image of the diabolo structure shown in Fig. 1b when the excitation is placed at the channel input (C<sub>i</sub>) for an incident beam polarized at (a) 0° and (b) 90°. The insets on the right display the signal from the right triangular area

with a 10x magnified color scale. Scale bars are 200 nm. **(c,d)** Simulated near-field SP transmittance maps corresponding to (a) and (b) respectively. A realistic discretized 2D model of the sample and a Gaussian beam (300-nm diameter,  $\lambda_{exc} = 810$  nm) are used. **(e)** Non-linear photoluminescence profiles extracted from (a) and (b) along the path indicated by the dash-dotted line in Fig. 2a. Inset: Magnified plot of the output (O) region corresponding to the dotted box in the main graph. **(f)** Histograms comparing the experimental non-linear luminescence intensity at the output O (full colored bars) with the near-field SP transmittance (striped orange bars) when the excitation beam is placed in either input I (left panel) or channel input Ci (right panel), for both  $0^\circ$  and  $90^\circ$  incident polarizations. The display of the SP transmittance is adjusted in each panel to match the largest experimental output of a given excitation location.

**Figure 5.** Transmission blockade by spectral mismatch in a non-symmetrical diablo. **(a)** SEM image of a non-symmetrical diablo structure composed of a small (630 nm side) and a large (730 nm side) triangles on the left (respectively right) of the 500 x 200 nm channel. **(b)** Full in-plane SP-LDOS map of the non-symmetrical diablo shown in (a). **(c, d)** nPL images of the non-symmetrical diablo structure shown in (a) when the excitation is placed in (I) for an incident beam polarized at (c)  $0^\circ$  and (d)  $90^\circ$ . **(e, f)** Simulated near-field SP transmittance maps corresponding to (c), (d) respectively. A realistic discretized 2D model of the sample and a Gaussian beam (300-nm diameter,  $\lambda_{exc} = 810$  nm) are used. **(g)** nPL profiles along the path indicated by the dash-dotted line in (a) for a series of polarization directions of the incident beam between  $0^\circ$  and  $94^\circ$ . The dashed box indicates the output O region. **(h)** Near-field transmittance spectra calculated at readout (O) for an excitation in (I) with a linearly polarized Gaussian beam at  $0^\circ$  (black squares) and  $90^\circ$  (red squares). The dash-dotted line indicates the experimental excitation wavelength (810 nm). In **(c-f)** the color scale of the signal from the right triangular area is magnified 10 times. All scale bars are 200 nm.

## References

- 1 Barnes, W. L., Dereux, A. & Ebbesen, T. W. Surface plasmon subwavelength optics. *Nature* **424**, 824-830, doi:10.1038/nature01937 (2003).
- 2 Engheta, N. Circuits with light at nanoscales: Optical nanocircuits inspired by metamaterials. *Science* **317**, 1698-1702, doi:10.1126/science.1133268 (2007).
- 3 Krasavin, A. V. & Zayats, A. V. Passive photonic elements based on dielectric-loaded surface plasmon polariton waveguides. *Appl. Phys. Lett.* **90**, doi:10.1063/1.2740485 (2007).
- 4 Ebbesen, T. W., Genet, C. & Bozhevolnyi, S. I. Surface-plasmon circuitry. *Phys. Today* **61**, 44-50, doi:10.1063/1.2930735 (2008).
- 5 Cai, W. S., White, J. S. & Brongersma, M. L. Compact, High-Speed and Power-Efficient Electrooptic Plasmonic Modulators. *Nano Lett.* **9**, 4403-4411, doi:10.1021/nl902701b (2009).
- 6 Wu, X. F. *et al.* On-Chip Single-Plasmon Nanocircuit Driven by a Self-Assembled Quantum Dot. *Nano Lett.* **17**, 4291-4296, doi:10.1021/acs.nanolett.7b01284 (2017).
- 7 Ma, H. F., Shen, X. P., Cheng, Q., Jiang, W. X. & Cui, T. J. Broadband and high-efficiency conversion from guided waves to spoof surface plasmon polaritons. *Laser Photon. Rev.* **8**, 146-151, doi:10.1002/lpor.201300118 (2014).
- 8 Oulton, R. F., Sorger, V. J., Genov, D. A., Pile, D. F. P. & Zhang, X. A hybrid plasmonic waveguide for subwavelength confinement and long-range propagation. *Nat. Photonics* **2**, 496-500, doi:10.1038/nphoton.2008.131 (2008).
- 9 Bozhevolnyi, S. I., Volkov, V. S., Devaux, E., Laluet, J. Y. & Ebbesen, T. W. Channel plasmon subwavelength waveguide components including interferometers and ring resonators. *Nature* **440**, 508-511, doi:10.1038/nature04594 (2006).
- 10 Volkov, V. S., Bozhevolnyi, S. I., Devaux, E., Laluet, J. Y. & Ebbesen, T. W. Wavelength selective nanophotonic components utilizing channel plasmon polaritons. *Nano Lett.* **7**, 880-884, doi:10.1021/nl070209b (2007).
- 11 Gramotnev, D. K. & Pile, D. F. P. Single-mode subwavelength waveguide with channel plasmon-polaritons in triangular grooves on a metal surface. *Appl. Phys. Lett.* **85**, 6323-6325, doi:10.1063/1.1839283 (2004).
- 12 Weeber, J. C. *et al.* Near-field observation of surface plasmon polariton propagation on thin metal stripes. *Phys. Rev. B* **64**, doi:10.1103/PhysRevB.64.045411 (2001).
- 13 Dionne, J. A., Sweatlock, L. A., Atwater, H. A. & Polman, A. Planar metal plasmon waveguides: frequency-dependent dispersion, propagation, localization, and loss beyond the free electron model. *Phys. Rev. B* **72**, doi:10.1103/PhysRevB.72.075405 (2005).
- 14 Kalavrouziotis, D. *et al.* 0.48Tb/s (12x40Gb/s) WDM transmission and high-quality thermo-optic switching in dielectric loaded plasmonics. *Opt. Express* **20**, 7655-7662, doi:10.1364/oe.20.007655 (2012).
- 15 Haffner, C. *et al.* All-plasmonic Mach-Zehnder modulator enabling optical high-speed communication at the microscale. *Nat. Photonics* **9**, 525-+, doi:10.1038/nphoton.2015.127 (2015).
- 16 Melikyan, A. *et al.* High-speed plasmonic phase modulators. *Nat. Photonics* **8**, 229-233, doi:10.1038/nphoton.2014.9 (2014).
- 17 Muehlbrandt, S. *et al.* Silicon-plasmonic internal-photoemission detector for 40 Gbit/s data reception. *Optica* **3**, 741-747, doi:10.1364/optica.3.000741 (2016).
- 18 Solis, D. *et al.* Electromagnetic Energy Transport in Nanoparticle Chains via Dark Plasmon Modes. *Nano Lett.* **12**, 1349-1353, doi:10.1021/nl2039327 (2012).
- 19 Teulle, A. *et al.* Multimodal plasmonics in fused colloidal networks. *Nat. Mater.* **14**, 87-94, doi:10.1038/nmat4114 (2015).
- 20 Ward, D. R., Huser, F., Pauly, F., Cuevas, J. C. & Natelson, D. Optical rectification and field enhancement in a plasmonic nanogap. *Nat. Nanotechnol.* **5**, 732-736, doi:10.1038/nnano.2010.176 (2010).
- 21 Stolz, A. *et al.* Nonlinear Photon-Assisted Tunneling Transport in Optical Gap Antennas. *Nano Lett.* **14**, 2330-2338, doi:10.1021/nl404707t (2014).
- 22 Emboras, A. *et al.* Atomic Scale Plasmonic Switch. *Nano Lett.* **16**, 709-714, doi:10.1021/acs.nanolett.5b04537 (2016).

- 23 Kern, J. *et al.* Electrically driven optical antennas. *Nat. Photonics* **9**, 582+, doi:10.1038/nphoton.2015.141 (2015).
- 24 Buret, M. *et al.* Spontaneous Hot-Electron Light Emission from Electron-Fed Optical Antennas. *Nano Lett.* **15**, 5811-5818, doi:10.1021/acs.nanolett.5b01861 (2015).
- 25 Parzefall, M. *et al.* Antenna-coupled photon emission from hexagonal boron nitride tunnel junctions. *Nat. Nanotechnol.* **10**, 1058+, doi:10.1038/nnano.2015.203 (2015).
- 26 Kinsey, N., Ferrera, M., Shalae, V. M. & Boltasseva, A. Examining nanophotonics for integrated hybrid systems: a review of plasmonic interconnects and modulators using traditional and alternative materials Invited. *J. Opt. Soc. Am. B-Opt. Phys.* **32**, 121-142, doi:10.1364/josab.32.000121 (2015).
- 27 Wei, H., Wang, Z. X., Tian, X. R., Kall, M. & Xu, H. X. Cascaded logic gates in nanophotonic plasmon networks. *Nat. Commun.* **2**, doi:10.1038/ncomms1388 (2011).
- 28 Viarbitskaya, S. *et al.* Tailoring and imaging the plasmonic local density of states in crystalline nanoprisms. *Nat. Mater.* **12**, 426-432, doi:10.1038/nmat3581 (2013).
- 29 Gu, L. *et al.* Resonant wedge-plasmon modes in single-crystalline gold nanoplatelets. *Phys. Rev. B* **83**, doi:10.1103/PhysRevB.83.195433 (2011).
- 30 Viarbitskaya, S. *et al.* Morphology-induced redistribution of surface plasmon modes in two-dimensional crystalline gold platelets. *Appl. Phys. Lett.* **103**, 131112, doi:10.1063/1.4823533 (2013).
- 31 Bellido, E. P. *et al.* Electron Energy-Loss Spectroscopy of Multipolar Edge and Cavity Modes in Silver Nanosquares. *ACS Photonics* **3**, 428-433, doi:10.1021/acsp Photonics.5b00594 (2016).
- 32 Huang, J. S. *et al.* Atomically flat single-crystalline gold nanostructures for plasmonic nanocircuitry. *Nat. Commun.* **1**, 150, doi:10.1038/ncomms1143 (2010).
- 33 Mejjard, R. *et al.* Advanced engineering of single-crystal gold nanoantennas. *Opt. Mater. Express* **7**, 1157-1168, doi:10.1364/ome.7.001157 (2017).
- 34 Cucho, A. *et al.* Modal engineering of Surface Plasmons in apertured Au Nanoprisms. *Sci Rep* **5**, 16635, doi:10.1038/srep16635 (2015).
- 35 Cucho, A. *et al.* Beyond dipolar regime in high-order plasmon mode bowtie antennas. *Opt. Commun.* **387**, 48-54, doi:10.1016/j.optcom.2016.11.013 (2017).
- 36 Xie, J. Y. *et al.* Ultracompact all-optical full-adder and half-adder based on nonlinear plasmonic nanocavities. *Nanophotonics* **6**, 1161-1173, doi:10.1515/nanoph-2017-0035 (2017).
- 37 Rousseaux, B. *et al.* Adiabatic passage mediated by plasmons: A route towards a decoherence-free quantum plasmonic platform. *Phys. Rev. B* **93**, doi:10.1103/PhysRevB.93.045422 (2016).
- 38 Roller, E. M. *et al.* Hotspot-mediated non-dissipative and ultrafast plasmon passage. *Nat. Phys.* **13**, 761+, doi:10.1038/nphys4120 (2017).
- 39 Kewes, G. *et al.* A realistic fabrication and design concept for quantum gates based on single emitters integrated in plasmonic-dielectric waveguide structures. *Sci Rep* **6**, doi:10.1038/srep28877 (2016).
- 40 Wang, S. M. *et al.* A 14 x 14  $\mu\text{m}^2$  footprint polarization-encoded quantum controlled-NOT gate based on hybrid waveguide. *Nat. Commun.* **7**, doi:10.1038/ncomms11490 (2016).
- 41 Bolisetty, S. *et al.* Amyloid-mediated synthesis of giant, fluorescent, gold single crystals and their hybrid sandwiched composites driven by liquid crystalline interactions. *Journal of Colloid and Interface Science* **361**, 90-96, doi:10.1016/j.jcis.2011.05.018 (2011).
- 42 Complementary experimental and simulated data are provided in Supplementary Information.
- 43 Teulle, A. *et al.* Scanning optical microscopy modeling in nanoplasmonics. *J. Opt. Soc. Am. B-Opt. Phys.* **29**, 2431-2437, doi:10.1364/JOSAB.29.002431 (2012).
- 44 Viarbitskaya, S., Demichel, O., Cluzel, B., des Francs, G. C. & Bouhelier, A. Delocalization of Nonlinear Optical Responses in Plasmonic Nanoantennas. *Phys. Rev. Lett.* **115**, 197401, doi:10.1103/PhysRevLett.115.197401 (2015).
- 45 Weeber, J. C. *et al.* Colloidal Quantum Dot Integrated Light Sources for Plasmon Mediated Photonic Waveguide Excitation. *ACS Photonics* **3**, 844-852, doi:10.1021/acsp Photonics.6b00054 (2016).
- 46 Rude, M., Simpson, R. E., Quidant, R., Pruneri, V. & Renger, J. Active Control of Surface Plasmon Waveguides with a Phase Change Material. *ACS Photonics* **2**, 669-674, doi:10.1021/acsp Photonics.5b00050 (2015).
- 47 Abb, M., Albella, P., Aizpurua, J. & Muskens, O. L. All-Optical Control of a Single Plasmonic Nanoantenna-ITO Hybrid. *Nano Lett.* **11**, 2457-2463, doi:10.1021/nl200901w (2011).

- 48 Lee, H. W. *et al.* Nanoscale Conducting Oxide PlasMOSter. *Nano Lett.* **14**, 6463-6468, doi:10.1021/nl502998z (2014).
- 49 Guo, P. J., Schaller, R. D., Ketterson, J. B. & Chang, R. P. H. Ultrafast switching of tunable infrared plasmons in indium tin oxide nanorod arrays with large absolute amplitude. *Nat. Photonics* **10**, 267-+, doi:10.1038/nphoton.2016.14 (2016).
- 50 Tame, M. S. *et al.* Quantum plasmonics. *Nat. Phys.* **9**, 329-340, doi:10.1038/nphys2615 (2013).
- 51 Li, C. X., Bolisetty, S. & Mezzenga, R. Hybrid Nanocomposites of Gold Single-Crystal Platelets and Amyloid Fibrils with Tunable Fluorescence, Conductivity, and Sensing Properties. *Adv. Mater.* **25**, 3694-3700, doi:10.1002/adma.201300904 (2013).

Preprint

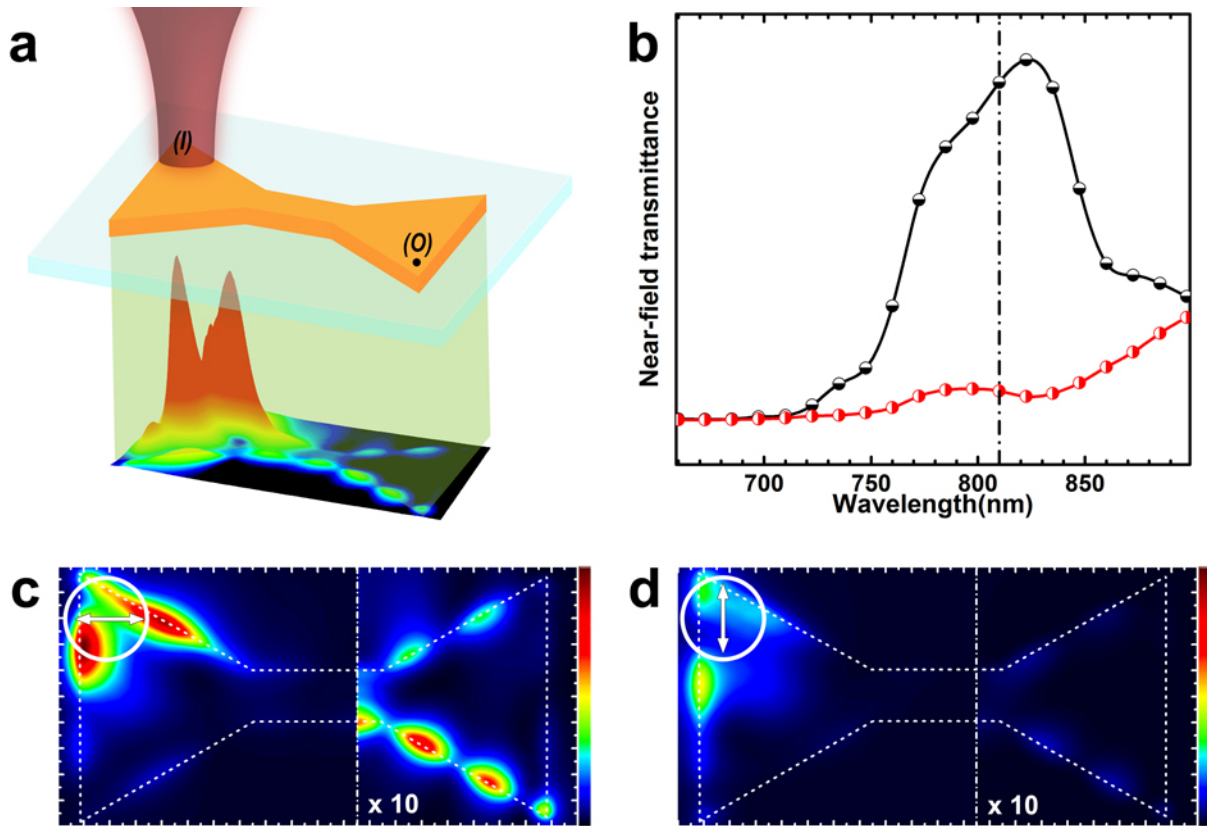


Figure 1  
U. Kumar et al.



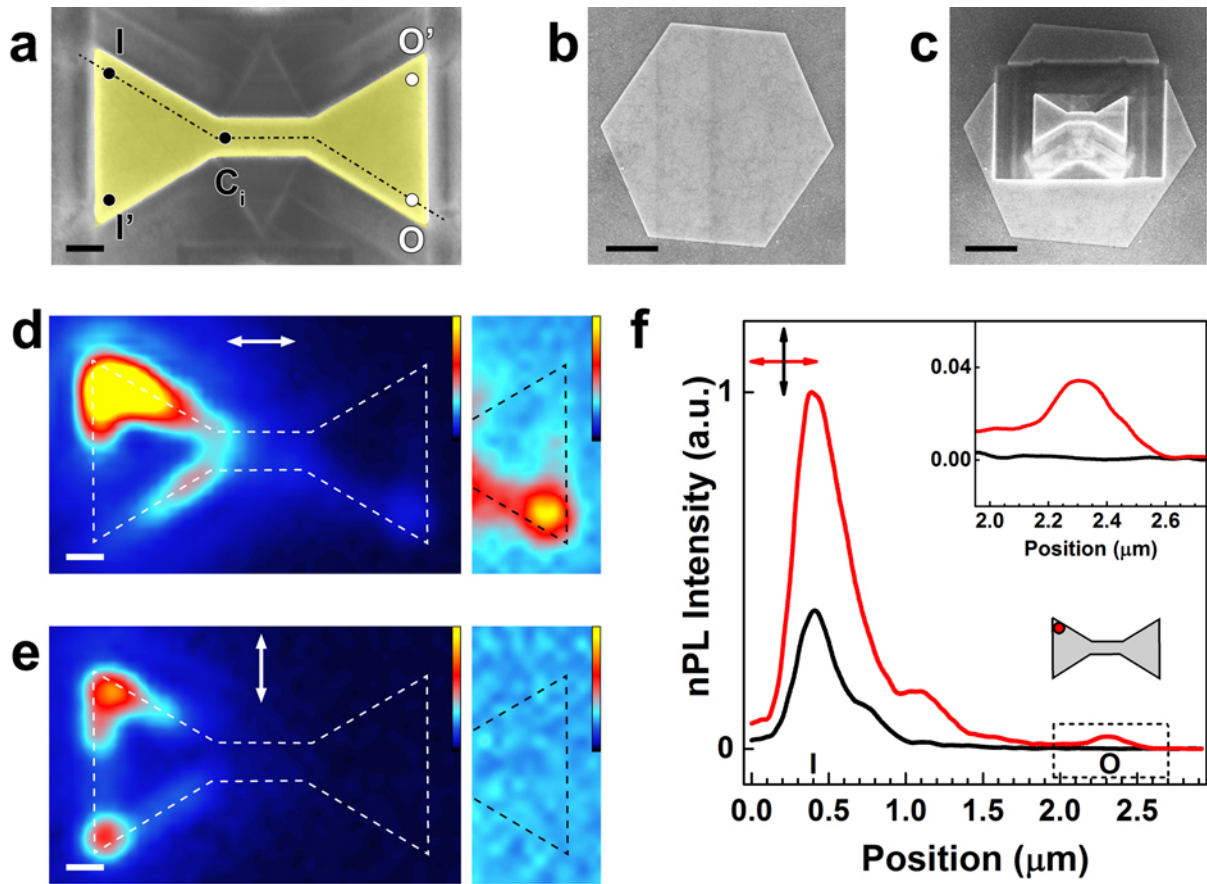


Figure 2  
U. Kumar et al.

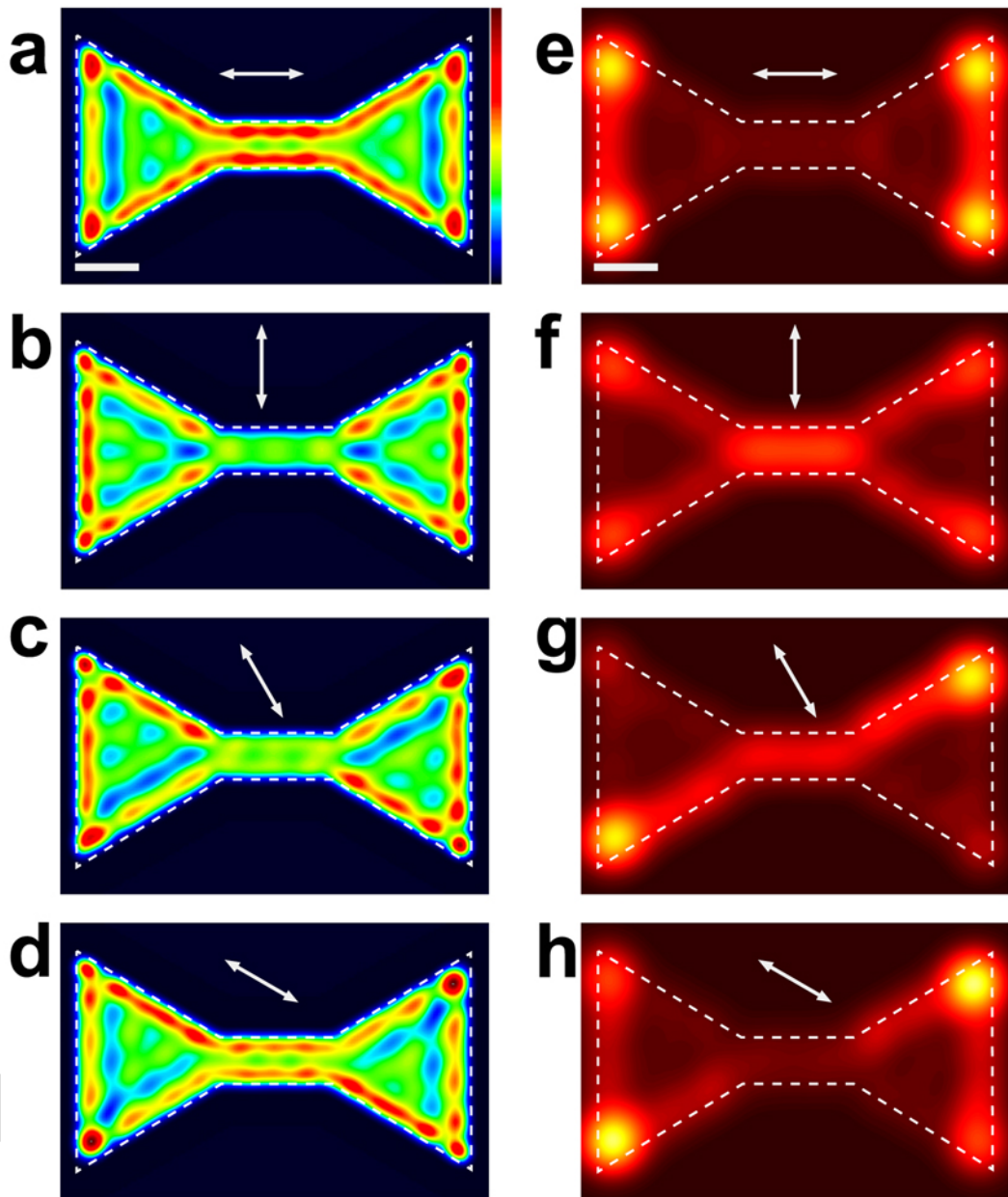


Figure 3  
U. Kumar et al.

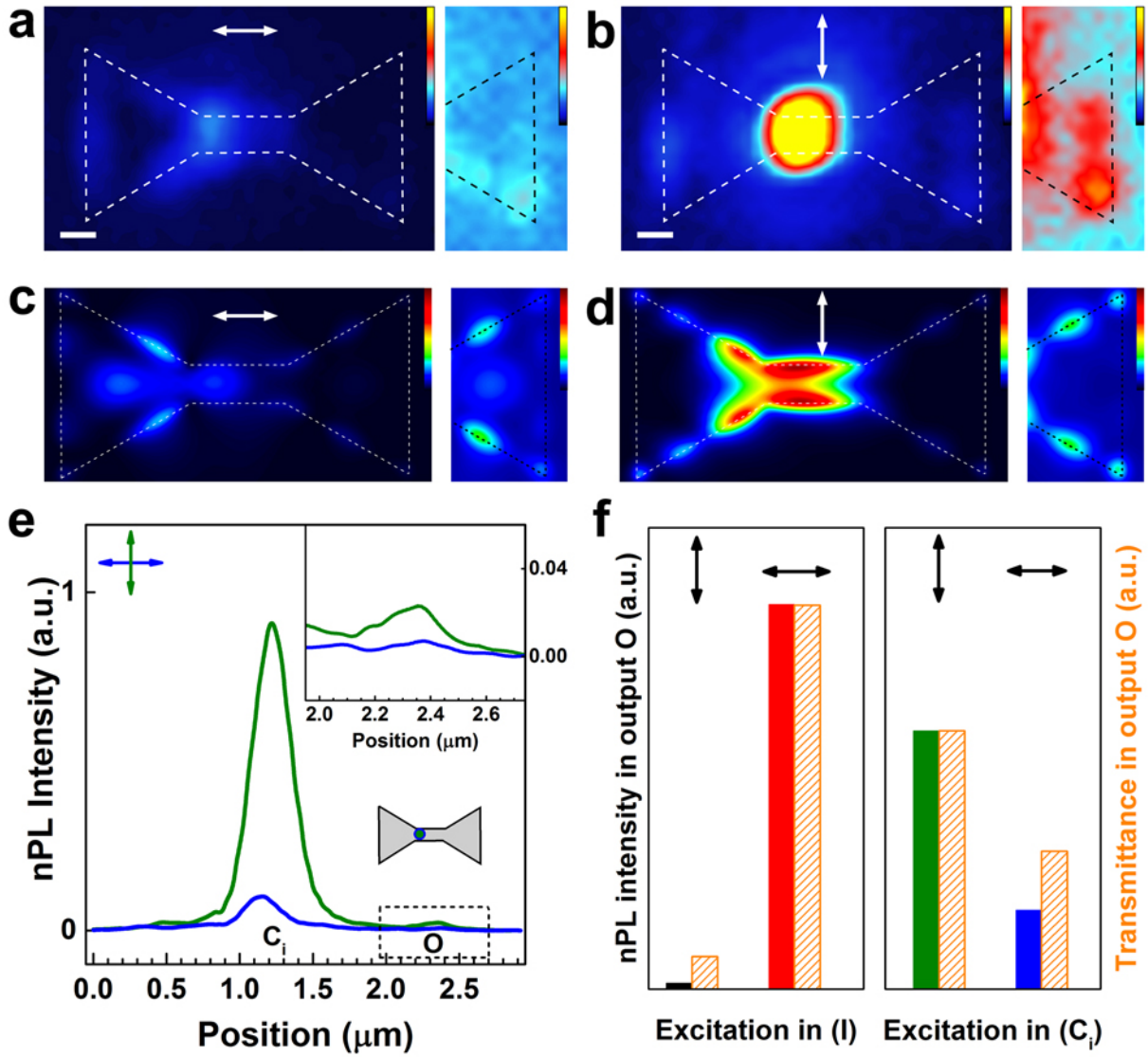


Figure 4  
U. Kumar et al.

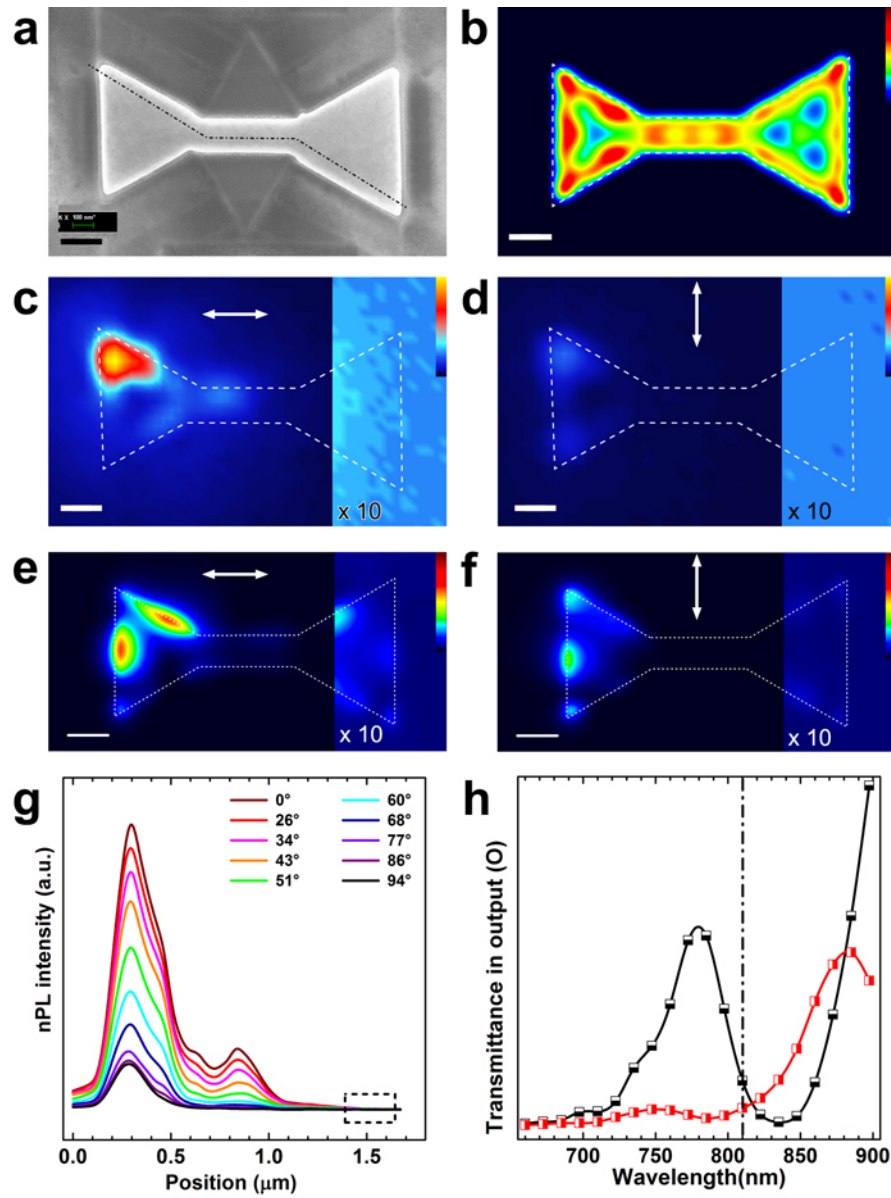


Figure 5  
U. Kumar et al.